

Dynamic modelling of overprinted impermeable fault gouges and surrounding damage zones as lower dimensional interfaces^{*,**}

Thomas Poulet^{a,b,*}, Martin Lesueur^c and Ulrich Kelka^d

^aCSIRO Mineral Resources, 26 Dick Perry Avenue, Kensington, WA 6151, Australia

^bSchool of Minerals and Energy Resources Engineering, UNSW Sydney, NSW 2052, Australia

^cCivil and Environmental Engineering, Duke, Durham, NC 27708-0287, USA

^dCSIRO Deep Earth Imaging Future Science Platform, 26 Dick Perry Avenue, Kensington, WA 6151, Australia

ARTICLE INFO

Keywords:

flow in fractured porous media
dynamic mixed permeability
lower dimensional interface
fault overprinting

ABSTRACT

In the modelling of subsurface fluid flow, faults are dominant features since they can act as fluid pathways or barriers. Special emphasis is therefore placed in representing them in a numerically efficient manner and the use of lower dimensional domains has become prevalent to simulate higher permeability features like fractures. Such features, however, only represent some of the components of natural fault networks, which can also include rather impermeable fault gouges surrounded by higher permeability damage zones for instance. Here we present a numerical approach to simulate such systems at a large scale, where the thickness of those features makes it advantageous to represent them as discrete rather than continuous domains, using lower dimensional interfaces in a conforming mesh. Benchmarks show excellent agreement with equivalent continuous simulations, regardless of the fault thickness or permeability, both for flow conduits and barriers. This approach can also account for the overprinting of faults with different permeabilities, as well as their dynamic evolution, which we illustrate with an example of trap charging. This work demonstrates the applicability of the approach to simulate fluid flow in faulted environments of various permeabilities and we discuss how those results can easily be extended to account for multi-physical processes.

1. Introduction

Fault networks are critical geological features that can control the fluid flow pattern in the upper crust above the brittle-ductile transition (Rawling, Goodwin and Wilson, 2001; Wibberley, Yielding and Toro, 2008; Faulkner, Jackson, Lunn, Schlische, Shipton, Wibberley and Withjack, 2010). As such, assessing the permeability of these structure and being able to accurately simulate flow and transport in these networks is of considerable interest in a number of fields including mineral exploration (Barnicoat, Sheldon and Ord, 2009) oil and gas production (Ferronato, Gambolati, Janna and Teatini, 2008), natural gas storage (Gasanzade, Bauer and Pfeiffer, 2019), CO_2 -storage (Tillner, Langer, Kempka and Kühn, 2016), or radioactive waste disposal (Tsang, Neretnieks and Tsang, 2015).

Due to complex hydraulic, mechanical and chemical interactions that occur in fault zones, these structures exhibit a wide range of permeability values, and can form flow conduits or barriers for instance. These scenarios represent two end members and combined barrier-conduit structures are likely to form in low-permeability strata (Bense and Person, 2006; Faulkner et al., 2010; Bauer, Schröckenfuchs and Decker, 2016). Field observations have also shown that porosity and permeability distributions in fault systems can be time-dependent, as active faults can experience short episodic periods of fluid flow triggered by seismic activity, followed by post-seismic healing (Louis, Luijendijk, Dunkl and Person, 2019). These dynamic permeability changes occur both ways, with increases also due to extensional fractures (Cappa, 2009) and decreases resulting from post-seismic healing (Aben, Doan, Gratier and Renard, 2017) or clay smear (Vrolijk, Urai and Kettermann, 2016). Those processes can be temporary, permanent, or episodic (Cox, 2016; Alevizos, Poulet and Veveakis, 2014), with opening and closing of porosities occurring at various time scales. Additionally, the sole consideration of different time scales can lead to a single feature forming both a barrier at human

* T.P. lead drafting the manuscript and developing the methodology. M.L. developed the interface implementation. U.K. provided the geological expertise. All authors contributed to the writing of the manuscript.

** Declarations of interest: None.

* Corresponding author

✉ thomas.poulet@csiro.au (T. Poulet)

ORCID(s): 0000-0001-7351-3083 (T. Poulet); 0000-0001-9535-2268 (M. Lesueur)

54 time scales and a pathway at geological times (Wibberley et al., 2008). This ambivalent behaviour clearly highlights
55 the importance of identifying and deepen our understanding of the fluid flow dynamics in fault networks.

56 Accurate flow and transport simulations in fault networks rely on appropriate discretization of the fault zone archi-
57 tecture, where the system should only be simplified as an end member (conduit or barrier) for problems where those
58 assumptions are perfectly justified. In this study we focus on common geological scenarios which include a mix of
59 permeability features, with a basic conceptual model comprising a low-permeability fault core (gouge) surrounded by
60 a more permeable damage zone (Caine, Evans and Forster, 1996; Barnicoat et al., 2009; Cappa and Rutqvist, 2011;
61 Faulkner et al., 2010; Sutherland, Toy, Townend, Cox, Eccles, Faulkner, Prior, Norris, Mariani, Boulton, Carpen-
62 ter, Menzies, Little, Hastings, Pascale, Langridge, Scott, Lindroos, Fleming and Kopf, 2012; Yamashita and Tsutsumi,
63 2017). This particular – yet quite wide-spread – case makes it unlikely to capture accurately regional fluid flow dynam-
64 ics by representing faults zones simply as conduits or barriers. Based on field observations in the Dixon Valley, Caine
65 et al. (1996) have estimated the permeability contrasts between host-rock, damage zone and fault core to be two to
66 three orders of magnitude. In such a case the faults act as transversal flow barriers but as longitudinal fluid conduits
67 and these individual structural elements need to be distinguished conceptually and treated accordingly when modelling
68 such scenarios.

69 In a subsurface system, fault cores represent geometrically thin features and the computational costs for resolving
70 such features numerically can be very high. This results both from the considerable number of fine mesh elements
71 required as well as the associated time-step size reduction to accommodate smaller elements. This fact led to the de-
72 velopment of various methods to model Discrete Fracture Networks (DFN), where the permeability of the host rock
73 matrix is negligible compared to the permeability of the thin features, or Discrete Fracture Methods (DFM), compro-
74 mising on the homogenisation simplification to still account for some of the matrix properties like its permeability
75 for instance. Efficient methods have been introduced to simulate thin features in a discrete manner (see review from
76 Berre, Doster and Keilegavlen, 2018), with their thickness or aperture not considered geometrically in the mesh, pro-
77 viding great numerical efficiency over the continuum approach where all features are considered and meshed explicitly.
78 Such techniques cover the whole spectrum of permeabilities, with some handling both the cases of fluid conduits and
79 barrier (e.g. Martin, Jaffré and Roberts, 2005; Angot, Boyer and Hubert, 2009). Even the pre-processing step of mesh-
80 ing the fracture or fault network has been greatly simplified with the development of powerful meshing packages
81 (e.g. Geuzaine and Remacle, 2009) for conforming methods accounting for all features in the mesh, as well as non-
82 conforming methods (e.g. Schädle, Zulian, Vogler, Bhopalam, Nestola, Ebigbo, Krause and Saar, 2019) which can
83 integrate those features without meshing them within the matrix.

84 A convenient concept to simulate thin features consists in considering them as lower-dimensional manifolds (Al-
85 boin, Jaffré, Roberts and Serres, 2002). This approach is gaining in popularity (see review from Berre et al., 2018)
86 and provides an efficient way to model highly permeable features, which is the most common end-member considered
87 when fractures are involved. From this perspective, considering other cases becomes a question of introducing extra
88 relevant constraints (Schädle et al., 2019), like imposing non-standard Robin type conditions at the interface to handle
89 flow barriers for instance (Martin et al., 2005).

90 In this contribution, we present an approach to simulate the fluid flow in barrier-conduit systems which comprise
91 faults of spatially and temporally varying permeabilities. Our proposed method accounts for the anisotropy associated
92 with fault zone architecture, distinguishing between longitudinal flow pathways (e.g. in the surrounding damage zone)
93 and transversal barriers across the fault core.

94 2. Method

95 Various methods exist to simulate conforming Discrete Fracture Matrix (DFM) models on conforming meshes,
96 as shown in the review from Berre et al. (2018). In this section, we start with a popular approach, showing some
97 of its strengths and weaknesses, before introducing additional degrees of freedom to palliate those deficiencies and
98 better simulate our specific problem or interest. Three discrete approaches are presented and compared to a reference
99 continuum case. The schematic of all methods is shown in Fig. 1 in 2D for clarity.

100 Among the numerous numerical platforms available, we chose to use the open-source REDBACK simulator (Poulet,
101 Paesold and Veveakis, 2017) to implement all features presented in this study, based on the Multiphysics Object Ori-
102 ented Simulation Environment (MOOSE) (Gaston, Newman, Hansen and Lebrun-Grandió, 2009). REDBACK was
103 specifically designed to investigate problems of fault reactivation (e.g. Veveakis, Alevizos and Poulet, 2017) and the
104 flexibility of MOOSE is particularly well adapted to develop new features independently of the dimensionality of the

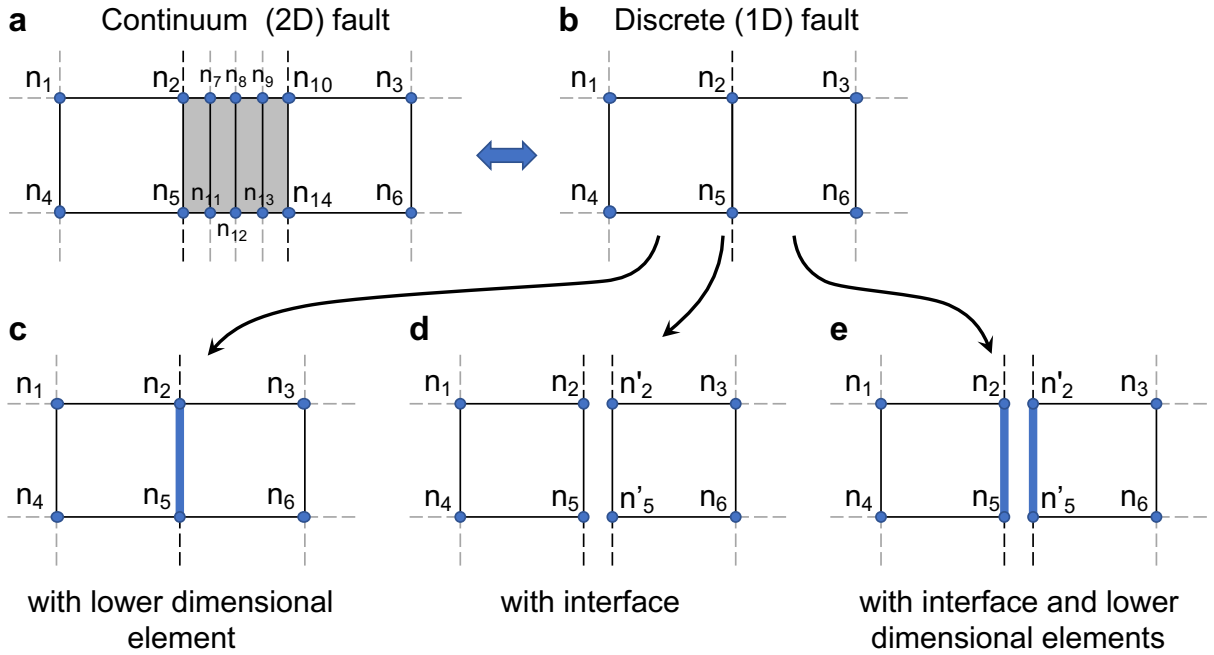


Figure 1: Schematics of the various mesh types used to model a fault, shown here in 2D between two quadrilateral elements; (a) Using 2D elements (in grey) to mesh the fault across its thickness, using an implicit continuum approach, used as reference in this study; (b) Using a discrete (1D) approach, with the fault handled at the common edge of the elements (nodes n_2 and n_5) in three various ways shown in the remaining subfigures; (c) 1D fault handled with additional lower-dimensional element between nodes n_2 and n_5 ; (d) 1D fault modelled by an interface between sets of duplicated nodes (n'_2 and n'_5) and their superposed counterparts (n_2 and n_5), shown here in exploded view (slightly shifted) for visualisation purposes; and (e) 1D fault modelled with both (i) an interface between the edge nodes (n_2 and n_5) and their superposed duplicated images (n'_2 and n'_5) in exploded view and (ii) lower-dimensional elements on the corresponding edges (n_2 - n_5 and n'_2 - n'_5).

105 meshes used and also to modify, where necessary, the meshes themselves, which were created in this study using
 106 GMSH (Geuzaine and Remacle, 2009).

107 2.1. Lower dimensional elements

108 A popular DFM method is using co-dimension one domains (Berre et al., 2018), to represent thin geological features
 109 like faults or fractures as infinitely thin geometries, while accounting for their actual thickness and behaviour through
 110 the system of equations solved. MOOSE provides this functionality to use lower dimensional domains inside the overall
 111 model (Schädle, Wilkins, Ebigbo and Saar), and this has been used for the purpose of modelling flow in fractured
 112 media (Cacace and Jacquey, 2017; Schädle et al., 2019). This method, shown in Fig. 1, removes an important level of
 113 complexity at the meshing stage and it is also numerically more efficient than the corresponding continuum method
 114 (Fig. 1a). Indeed, avoiding elements of very small size to discretise the thickness of the fault not only reduces the total
 115 number of elements but also increases accordingly the timestep size that can be used in the simulation. An additional
 116 set of co-dimension one elements are added as a new subdomain to the mesh to connect the existing nodes on the
 117 fault (n_2 and n_5 on Fig. 1c), superposed to the face of existing elements. Any system of equations can be solved on
 118 such subdomains, which provides an easy and powerful way to run for example complex multi-physics simulations
 119 (e.g. Cacace and Jacquey, 2017). For the purpose of comparing methods, we restrict ourselves to the simplest case of
 120 hydraulic diffusion, which can simply be described in dimensionless form as

$$\partial_t p = D \partial_i \partial_i p \quad (1)$$

121 where P denotes the dimensionless pore pressure, t the dimensionless time and D the diffusivity.

122 To account for the mixed dimensionality of the various subdomains in the variational formulation, all terms inte-
 123 grated on the lower dimensional elements need to be multiplied by the thickness of the fault or aperture of the fracture,
 124 a , as described in (Schädle et al.). For the diffusion term, the same effect can be obtained by using a diffusivity value
 125 scaled by the same factor a .

126 This method allows accurate modelling of highly permeable faults with longitudinal flow, but it is not designed to
 127 model transversal flow, since the lower dimensional elements are infinitely thin and therefore "invisible" transversally.
 128 This issue has been addressed (e.g. Martin et al., 2005) to model flow barriers as well as fractures, and this can be
 129 achieved in MOOSE by enriching the problem with an additional constraint on the transversal flow, creating *interfaces*
 130 on the faults to account for the transition between both sides of each fault.

131 2.2. Interface

132 Simulating transversal flow across an infinitely thin feature requires extra constraints (e.g. Martin et al., 2005;
 133 Angot et al., 2009) with a discontinuous approach, where all nodes on the fault are duplicated and superposed, as
 134 shown on Fig. 1d. Note that this figure is shown in exploded view, so all pairs of duplicated nodes (n_i and n'_i) can
 135 be distinguished visually. This approach can be easily implemented in MOOSE through its *interface* functionality,
 136 following (Lesueur, 2019), where the contribution to the variational form can be described between pairs of duplicated
 137 nodes, in this instance expressing the continuity of flux between the regions on each side of the interface, replacing the
 138 middle region R_3 on Fig. 2.

139 The method presented in the previous paragraph focused on describing permeable faults or fractures but this rep-
 140 represents only one half of the spectrum. Another very interesting feature of faults is their ability to seal off fluids when
 141 their permeability is very low. However, the problem of flow barriers is radically different from fluid conduits and
 142 the lower-dimensionality method is not adapted to deal with those system. Specifically, the fluid flow is controlled in
 143 this case by the transversal low diffusivity of the fault that needs to be precisely modelled. This paragraph presents an
 144 approach to solve fluid flow through a very low permeability fracture. Since an impermeable fault gouge is a relatively
 145 thin feature, the flow in the fault is considered to always remain in steady-state.

146 When modelled as a flat interface as intended for numerical cost, the flow barrier results in a discontinuity of
 147 pressure at the fault core. In order to handle discontinuities at the interface, we duplicate nodes at the interface, that
 148 still superpose at the same coordinate. Each node represents one side of the interface and the relationship between
 149 those two duplicated nodes is given by a prescribed interface law. In the case of hydraulic diffusion, the interface law
 150 is simply derived from the continuity of flux across each side of the interface, expressed as

$$D^{(R)} p_{,i}^{(R)} n_i^{(F)} = D^{(F)} p_{,i}^{(F)} n_i^{(F)}, \quad (2)$$

151 where the superscripts (F) and (R) refer to the fault (interface) and neighbouring regions (reservoir) respectively.

152 The gradient of pressure between the two sides of the interface (F) of effective thickness a , denoted by the exponents
 153 (A) and (B), is computed as

$$p_{,i}^{(F)} n_i^{(F)} = \frac{\Delta p}{a} = \frac{p^{(A)} - p^{(B)}}{a}. \quad (3)$$

154 Combining Eqs. 3 and 2 we end up with a relationship for the interface law defined as:

$$D^{(A)} p_{,i}^{(A)} n_i^{(F)} - D^{(F)} \frac{p^{(B)} - p^{(A)}}{a} = 0, \quad (4)$$

$$D^{(B)} p_{,i}^{(B)} n_i^{(F)} - D^{(F)} \frac{p^{(B)} - p^{(A)}}{a} = 0. \quad (5)$$

155 Implementing the interface law for diffusion in a finite element code consists in adding the second term of the equations
 156 above to the respective residuals of node (A) and node (B), as the first term represents the natural boundary conditions
 157 for diffusion at the interface.

158 To verify the implementation of this pore pressure interface, we compare the results against an analytical problem
 159 for a simple one-dimensional case. We consider three regions (R_1 , R_2 , R_3) of various thicknesses (D_1 , D_2 , D_3) and
 160 permeability values (k_1 , k_2 , k_3), and solve for the steady-state of the 1D horizontal flow through as (Fig. 2). We apply

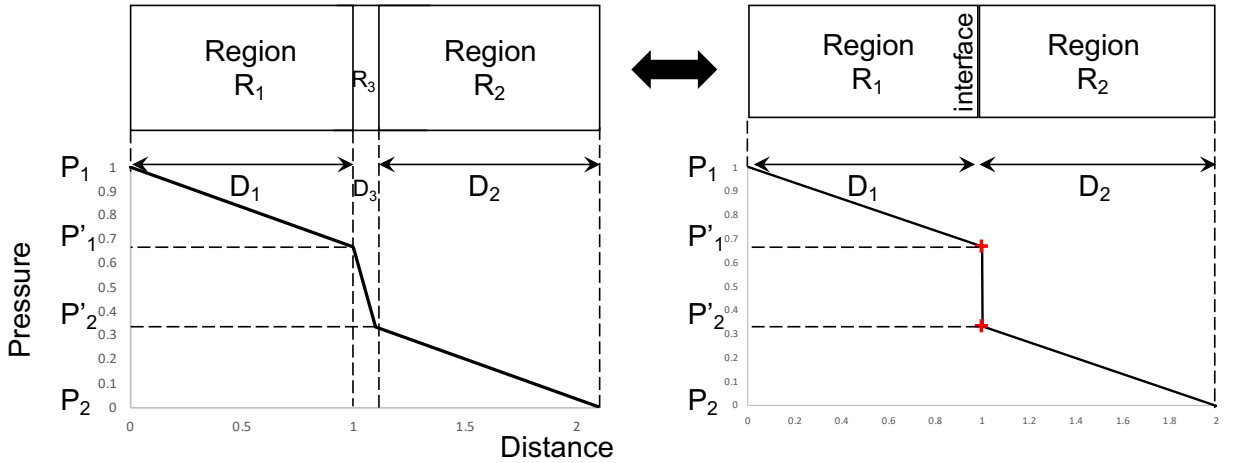


Figure 2: Model used to benchmark the flow interface. The specific case plotted is described by $D_1 = D_2 = 10 \times D_3$; $p_1 = 1$ and $p_2 = 0$; $k_1 = k_2 = 10 \times k_3$. On the left are plotted the result for the system fully resolved and on the right for the reduced system with interface. The system with interface matches with machine precision the results of the full system, highlighted with the red crosses.

161 a pressure gradient across these three blocks with constant boundary conditions at each end (p_1 and p_2). The two
 162 pressures p'_1 and p'_2 at the interface between the regions 1-3 and 2-3 can be expressed as:

$$p'_2 = \frac{k_1 k_3 D_2 D_3 p_1 + k_2 D_3 (k_1 D_3 + k_3 D_1) p_3}{(k_3 D_2 + k_2 D_3) * (k_1 D_3 + k_3 D_1) - k_3 k_3 D_1 D_2}, \quad (6)$$

$$p'_1 = \frac{k_1 D_3 p_1 + k_3 D_1 p'_2}{k_1 D_3 + k_3 D_1}. \quad (7)$$

163 This analytical solution is used to validate the numerical results obtained by solving a similar problem where
 164 the middle region is replaced by a flat interface, with the setup and results shown in Fig. 2, demonstrating perfect
 165 agreement. More detailed benchmark results are presented in Sec. 3.

166 We note that compared to the lower-dimensional approach, which was *kernel* agnostic, this method requires a
 167 specific translation to an interface law for each physical process considered. Still, adding more complexity is not
 168 complicated and we demonstrate this by adding gravity effects to the interface law for Darcy's law. Eq. 5 becomes:

$$-\frac{k^{(A)}}{\mu_f} (p_{,i}^{(A)} - \rho_f g_i) n_i^{(F)} + \frac{k^{(F)}}{\mu_f} \left(\frac{p^{(B)} - p^{(A)}}{a} - \rho_f g_i n_i^{(F)} \right) = 0, \quad (8)$$

$$-\frac{k^{(B)}}{\mu_f} (p_{,i}^{(B)} - \rho_f g_i) n_i^{(F)} + \frac{k^{(F)}}{\mu_f} \left(\frac{p^{(B)} - p^{(A)}}{a} - \rho_f g_i n_i^{(F)} \right) = 0. \quad (9)$$

169 2.3. Combining lower dimensional elements and interface

170 With the lower dimensional subdomains of Sec. 2.1 capturing longitudinal flow and the interface of Sec. 2.2 han-
 171 dling transversal flow barriers, we now combine both approaches to simulate any combination of fault permeabilities.
 172 In particular, we target the case of sealing fault cores bordered by permeable damage zones on either side by using
 173 the approach shown schematically in Fig. 1e, with an interface between duplicated set of nodes along the fault, along
 174 with one extra lower dimensional subdomain on either side of the fault. This particular setup allows to simulate the
 175 longitudinal flow independently on either side of a barrier, with the sum of the scaling factors for both subdomains
 176 (see Sec. 2.1) adding up to the thickness a of the fault. Without any specific information, both are taken as $a/2$. This
 177 approach is tested and compared to the previous two in a series of benchmarks presented in Sec. 3.2.

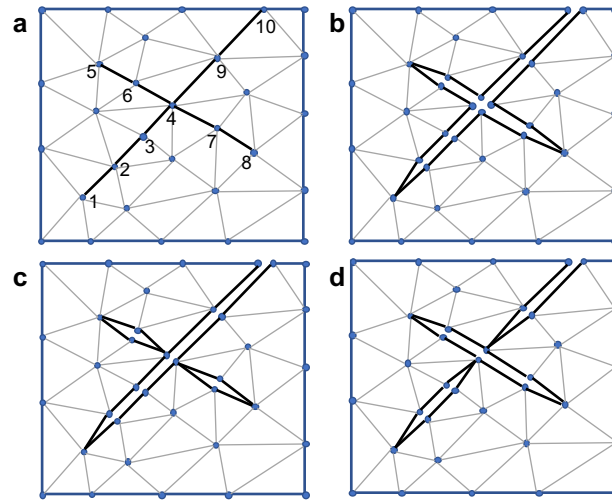


Figure 3: Schematic of node splitting for handling fault connections and intersections; (a) initial mesh, with two intersecting sets of edges (involving 10 nodes) marked as faults; (b) corresponding mesh topology after node splitting, with some nodes duplicated (and superposed, but shown shifted for visualisation purposes) once (nodes 2, 3, 6, 7, 9, 10) or three times (node 4); nodes (1,5,8) at the extremities of the faults but not on the boundaries are not duplicated; (c) and (d) both possible cases of fault overprinting with extremity node (4) duplicated only once.

2.4. Mesh generation

To use this approach, some interfaces with duplicated nodes need to be added to the original mesh, along with a pair of lower dimensional subdomains on either side of those interfaces, paying particular attention to the cases of faults intersections. While this step represents conceptually a pre-processing step independent from the simulation itself, we implemented in REDBACK a functionality as a *MeshGenerator* to generate such a mesh from an original one where faults are simply tagged as *sidesets*. This function can handle the cases of faults cross-cutting the domain boundaries and intersecting each other, either fully or partially. Those cases are conceptually displayed in Fig. 3. Fig. 3a shows an example of a 2D mesh with two faults intersecting each other, one of which touches the top boundary. Fig. 3b shows the equivalent exploded view, with all nodes on the original faults duplicated, except at fault extremities not on the boundary (nodes 1, 5 & 8). In this example, the node (index 4) at the intersection of both faults ends up duplicated three times. Fig. 3b&c show how to handle cases of fault overprinting. The intersecting node is only duplicated for the latest geological fault, allowing longitudinal flow through the intersection along that fault. The other (earlier) one needs to be defined in two parts, one on each side.

3. Results & discussion

In this section we showcase the capabilities of the approach presented in Sec. 2, to model faults of various permeabilities – flow channels and barriers – as lower dimensional interfaces, through several benchmarks and applications.

3.1. Generic example

To begin with, we illustrate the approach by solving the transient pressure diffusion problem (eq. 1) on a 3D block of size 1 containing three discrete faults of thickness 0.001, shown in Fig. 4a. The faults are five times more permeable than the matrix along their surfaces (see Sec. 2.1), but with a transversal permeability (across their thickness) which is ten times lower than the matrix. Starting from a uniform zero pressure in the model, a constant dimensionless pressure value of 1 is imposed at the bottom of the model and Fig. 4b shows the typical patterns obtained from fracture flow through highly permeable features. Fig. 4c, however, which displays pressure profiles on the faults only, highlights the effect of the transversal permeability, with the pressure diffusing faster around the fault than across them. To better understand the impact of the longitudinal and transversal permeabilities, some quantitative benchmarks are required.

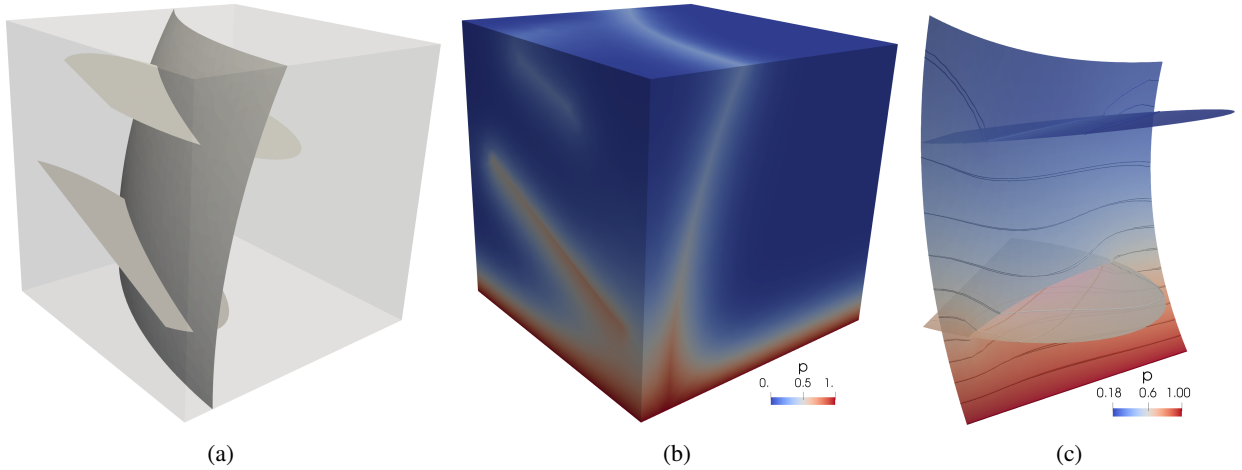


Figure 4: Generic scenario of pressure diffusion in a faulted block. (a) Geometry, two oval faults intersecting a curved fault (as the implementation is not restricted to linear features). (b) Pressure profile highlighting the high longitudinal permeability of the faults. (c) Pressure contours on the faults (rotated view), highlighting the lower transversal permeability of the faults. Note the apparent duplication and shift of the isobaric lines, which emphasises the differential of pressure between the two faces of the fault.

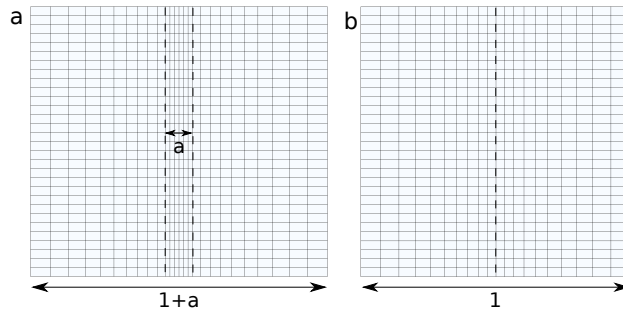


Figure 5: Benchmark meshes used for the (a) continuum approach, with a vertical fault of aperture a meshed in the centre, and (b) discrete approach, with a vertical fault indicated by a dashed line at the interface between two columns of mesh elements.

3.2. Benchmarks

203 Various benchmarks have been proposed to assess fluid flow implementations through thin features, faults or frac-
 204 tures (e.g. Shao, He, Hokr, Gardner, Kunz and Balvin, 2016; Hokr, Shao, Gardner, Balvín, Kunz, Wang and Vencl,
 205 2016; Cacace and Jacquy, 2017), yet they most often focus distinctly either on conduits or barriers, but not neces-
 206 sary on a mix of both. We propose therefore to test our approach on a simple scenario of hydraulic diffusion through
 207 a 2D rectangular domain containing a single feature, to compare the effects of the various implementations on the
 208 longitudinal and transversal flow components.
 209

3.2.1. Setup

210 We solve the problem of dimensionless pressure diffusion (eq. 1) on a 2D unitary square, for clarity, containing a
 211 single vertical feature in its centre (Fig. 5). This geometry is meshed in two different manners, using the continuum
 212 and discrete approaches presented in Sec. 2. With the continuum approach, shown in Fig. 5a, the feature of thickness a
 213 is represented explicitly with its true thickness and meshed as the other regions of the domain, leading to a total width
 214 of the domain of dimension $1 + a$. On the other hand, the discrete approach, shown in Fig. 5b, only represents the
 215 thin feature implicitly (shown in dashes on the figure) in between the two central columns of elements, keeping a total
 216 width of 1. The matrix surrounding the central feature is meshed identically for both types of meshes, with each half
 217 of the domain represented by 10×30 elements (see Fig. 5). For the continuum approach, the central feature is meshed
 218

219 with six elements across.

220 In all cases, a constant initial pressure is prescribed over the whole domain ($P_{init} = 0$) and two sets of boundary
 221 conditions (BC) are used to compare the longitudinal and transversal flows, by setting a constant over-pressure ($P = 1$)
 222 either on the top or on the left boundary. Three cases are investigated, for a diffusivity within the central feature (D_f)
 223 which is ten times larger, equal to, or ten times lower than the diffusivity of the surrounding matrix (D_m). The resulting
 224 effects are then compared on two different meshes, for fault thicknesses $a = 0.01$ and $a = 0.1$. The following three
 225 subsections present the results of the methods described in Sec. 2.1, 2.2 and 2.3 on the 12 respective cases (2 boundary
 226 conditions \times 2 fault thicknesses \times 3 diffusivity contrasts), all compared with the reference results obtained with the
 227 continuum approach, in which the fault thickness is explicitly accounted for in the mesh.

228 In order to test the implementation of the time dependency, all benchmarks are performed on a transient simulation,
 229 for an arbitrary total dimensionless time $t_{end} = 5$ with a time step $dt = 0.1$. To evaluate the results, the pressure profiles
 230 are plotted on a horizontal cross-section at mid-height, i.e. on a profile perpendicular to the fault at $y = 0.5$. The results
 231 obtained with discrete approaches are superposed across the matrix on top of the reference results computed with the
 232 continuum approach, leaving a gap across the fault where the pressure is not resolved.

233 3.2.2. Lower dimensional elements

234 First, we simulate the flow diffusion in the discrete approach using only lower dimensional elements, following
 235 the method described in Sec. 2.1 and the results are shown in Fig. 6. As expected, all subfigures for longitudinal flow
 236 (top BC, white backgrounds) show perfect matches between the discrete and continuum results, regardless of the fault
 237 thickness (which is irrelevant in that case) or diffusivity contrast between the fault and the matrix. The subfigures
 238 for transversal flow (left BC, grey backgrounds), however, demonstrate the limitations of this method, which is only
 239 valid for transversal flow across highly diffusive faults but does not capture the effect of a fault with equal or lower
 240 permeability than the matrix, with the discrepancy dramatically increasing as the fault thickness increases (e.g. Fig. 6j).

241 3.2.3. Interface

242 Next, we run the same set of scenarios using the discrete method presented in Sec. 2.2, which was designed to
 243 account for flow barriers. Fig. 7 shows the comparison of the results against the respective solutions obtained with
 244 the continuum approach. These results show that the method captures indeed most of the effects of flow barriers
 245 for transversal flow (left BC, grey backgrounds), with a discrepancy remaining due to the transient effects not being
 246 appropriately accounted for, that becomes more obvious with increasing fault thickness. The method does not capture
 247 at all any effect of longitudinal flow (top BC, white backgrounds) if the fault diffusivity differs from the matrix one.

248 3.2.4. Combined Interface and lower dimensional elements

249 Finally, we test the same scenarios using a combination of the two previous methods, as described in Sec. 2.3.
 250 Fig. 8 shows perfect agreement for every single case, regardless of the fault thickness, diffusivity contrast between the
 251 fault and matrix, or direction of the flow. This approach captures very well the longitudinal flow thanks to the lower
 252 dimensional elements, but also the transversal flow thanks to the interface. Note that the appropriate handling of the
 253 transience from the lower dimensional elements also eliminates the small discrepancy observed for transversal flow in
 254 Sec. 3.2.3.

255 3.3. Mixed permeability contrasts

256 After the validation of the approach on a simple benchmark of Sec. 3.2, we now look at an example to illustrate
 257 an application involving two intersecting faults of different permeabilities, respectively 100 times higher and lower
 258 than the value the permeability for the matrix background. We solve the flow on a unit square with Dirichlet boundary
 259 conditions for the dimensionless pressure on the left-hand side ($P = 1$) and right-hand side ($P = 0$) of the model. The
 260 sealing fault crosses the whole height of the model and is intersected by the more transmissive one, as shown on Fig. 9.
 261 Following Sec. 2.3, the overprinting of one fault by the other is important to consider and both scenarios are therefore
 262 presented.

263 Fig. 10 shows the results obtained using both the discrete approach of Sec. 2.3 (Fig. 10c&d) and a continuum
 264 approach, for reference, in which the faults are meshed across their thickness (Fig. 10a&b). Both meshes have a
 265 relatively fine mesh, with a similar number of triangles ($\approx 24,000$ for the discrete one and $\approx 25,000$ for the continuum
 266 one). Fig. 10a&c show the results for the case where the sealing fault overprints the other and forms a complete flow
 267 barrier, while Fig. 10b&d represent the other case where the permeable fault provides a channel piercing through the

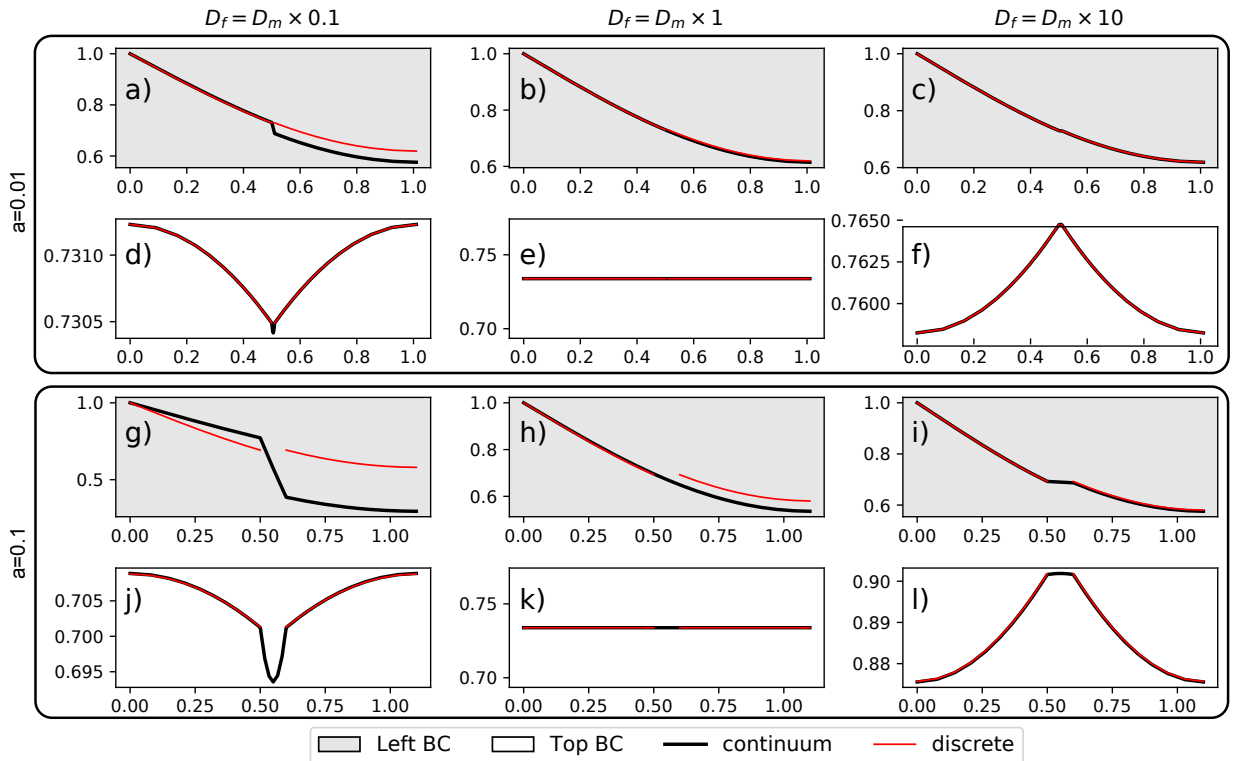


Figure 6: Benchmark results comparing the continuum (black line) and discrete (red line) cases for the lower dimensional implementation on two different geometries, with a fault thickness of $a = 0.01$ (a-f) and $a = 0.1$ (g-l), as described on Fig. 5. The three columns show various cases of fault diffusivity (D_f), respectively smaller than, equal to, and larger than the matrix diffusivity (D_m). All profiles show the pressure (y-axis) on a horizontal cross-section (x-axis) at mid-height of the model. Two sets of fixed pressure boundary conditions were used to force a flow from the left (grey background) or from the top (white background). Results show good agreement for the case of top flow, but the fault remains invisible to any transversal flow (from the left, white backgrounds).

268 barrier. The results are in perfect agreement, as illustrated by the identical patterns of the isobars between the top and
 269 bottom rows of Fig. 10, showing only the difference of thickness of the fault where the permeable feature ends, towards
 270 the upper centre of the model.

271 3.4. Trap charging

272 Finally, we demonstrate an illustrative scenario of fault reactivation for a 3D reservoir within an antiform, in the
 273 shape of a dome, intersected by and displaced along a 60° dipping fault, inside a unit cube bounding box, which
 274 showcases the ability to model dynamic permeability changes. The permeability of the reservoir is taken as reference
 275 with a normalised diffusivity of $D_{res} = 1$, corresponding to a permeability value of 0.1 D. The rest of the volume is
 276 mostly taken as more impermeable, to be representative of a cap rock, with a diffusivity of 10^{-4} (0.01 mD), except
 277 for the fault which is modelled using the approach described in Sec. 2.3. The transversal diffusivity of the fault is
 278 considered to be 10^{-6} (0.1 μ D), representing a barrier, while the longitudinal diffusivity of the fault on either side is
 279 taken as 10^4 (1,000 D), representing some more permeable damaged zones very close to the fault. Note that all values
 280 are presented in dimensionless forms as the purpose of this study is to highlight the capabilities of the method rather
 281 than simulate a realistic geological scenario. The pressure is initialised with a 0 value at the top of the model and a
 282 hydrostatic gradient.

283 In this scenario, we simulate qualitatively the two important phases of a reservoir forming in a trap and discharging
 284 due to the fault reactivation (Wibberley et al., 2008), accounting for Darcy flow and gravity (Eqs. 8&9 for the interface
 285 law). The trap charging involves a pressure build-up within the lower part of the reservoir, taking place at geological
 286 time scales. The very short fault reactivation event, on the other hand, sees an abrupt increase of the transversal

Flow in faulted reservoirs

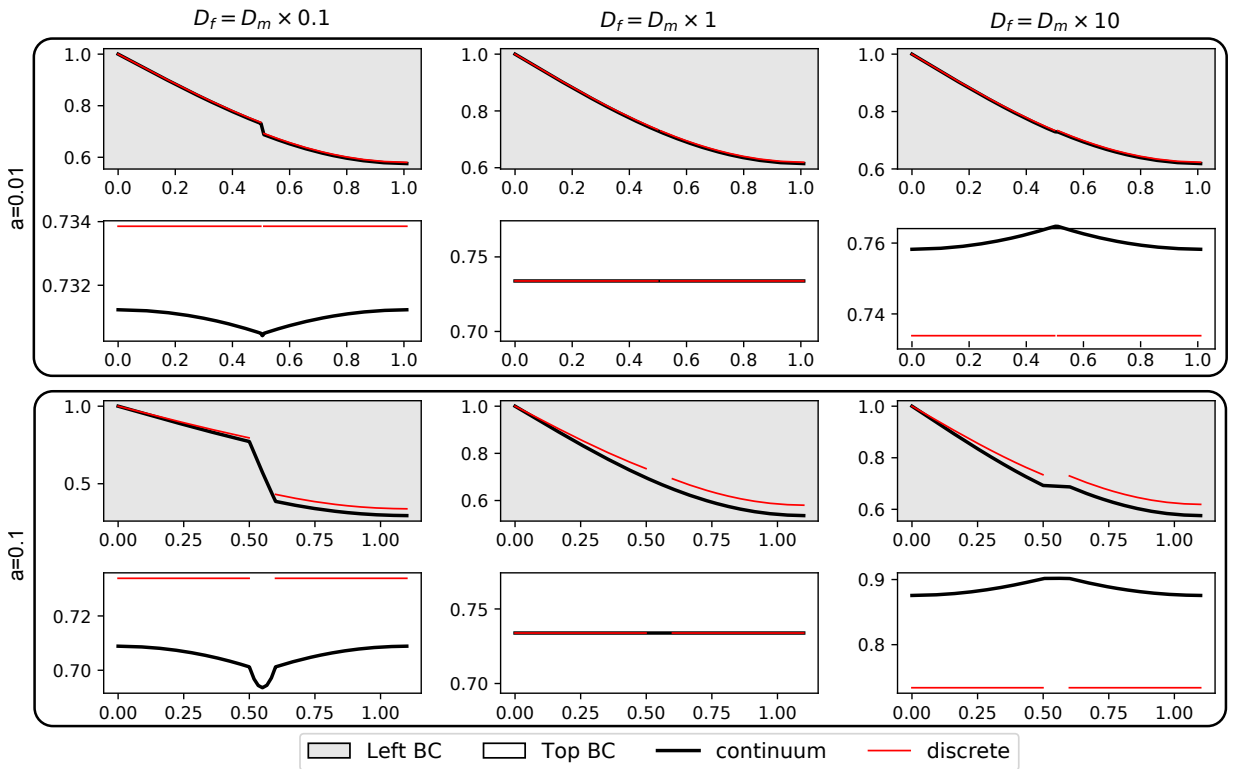


Figure 7: Benchmark profiles for interface implementation showing appropriate handling for horizontal flow (left BC, grey background), increasingly better as the fault gets thinner (smaller a). The longitudinal diffusivity, however, is not accounted for and the fault remains invisible from the top (top BC, white backgrounds).

287 permeability of the fault, leading to displacement of the over-pressurised fluid to the upper part of the reservoir, forming
 288 the next trap. A Neumann boundary condition – constant flux – for the dimensionless pressure is applied on left face of
 289 the bottom part of the reservoir for the whole duration of the simulation, from $t = -1, 200, 00$ a to $t = 600, 000$ a. At
 290 $t = 0$, the transversal diffusivity of the fault is artificially increased by four orders of magnitude (Nguyen, Guglielmi,
 291 Graupner and Rutqvist, 2019) to 1 mD, in order to simulate a seal failure during a fault reactivation event.

292 Fig. 11 and 12 show three snapshots of the simulation results for the pressure and fluid flow, at various times
 293 during the simulation. Fig. 11a shows the pressure distribution in the model after the first timestep (when the flow
 294 just started charging the lower part of the reservoir). Fig. 11b shows the pressure just before the fault reactivation (at
 295 $t = 0$), highlighting the pressure build-up in the lower part of the reservoir, with fluid flowing along the fault, but
 296 barely entering the upper part of the reservoir, mostly – but not completely – sealed by the fault. Fig. 11c at the end of
 297 the simulation, when the upper part of the reservoir has already been charged considerably. Fig. 12a and Fig. 12c show
 298 the corresponding fluid flow velocities at the beginning and end of the simulation, where only the input flow boundary
 299 condition is visible, while Fig. 12b shows the flux slightly after reactivation, at $t = 8, 000$ a, when the overpressure from
 300 the closest part of the lower reservoir to the fault is triggering some equilibration flow to the upper part of the reservoir
 301 near the (now transmissive) fault. Fig. 13 shows the pore pressure evolution at two sampling points on either side of
 302 the fault, in the upper part of the model, with the same coordinates (since the fault is infinitely thin) highlighted by the
 303 small grey point on Fig. 11. Fig. 13a shows the results during the whole simulation and Fig. 13b zooms in around the
 304 reactivation event. Those results show clearly the trap charging in the lower part of the reservoir over long time scales,
 305 as well as the effects of the abrupt fault reactivation, leading to a large transversal permeability increase of the fault,
 306 followed by the consequent charging of the upper part of the reservoir. The pressure is naturally building up much
 307 more rapidly in the zones connected by high permeability until reactivation, with Fig. 13a highlighting the pressure
 308 differential building across the fault in the upper part of the reservoir, before both sides equilibrate during a short time
 309 dictated by the fault thickness and its increased permeability. The pressure equilibration of Fig. 13b correspond to the
 310 flow distribution of Fig. 12b. Note that before the reactivation ($t < 0$) the pressure in the upper reservoir along the

Flow in faulted reservoirs

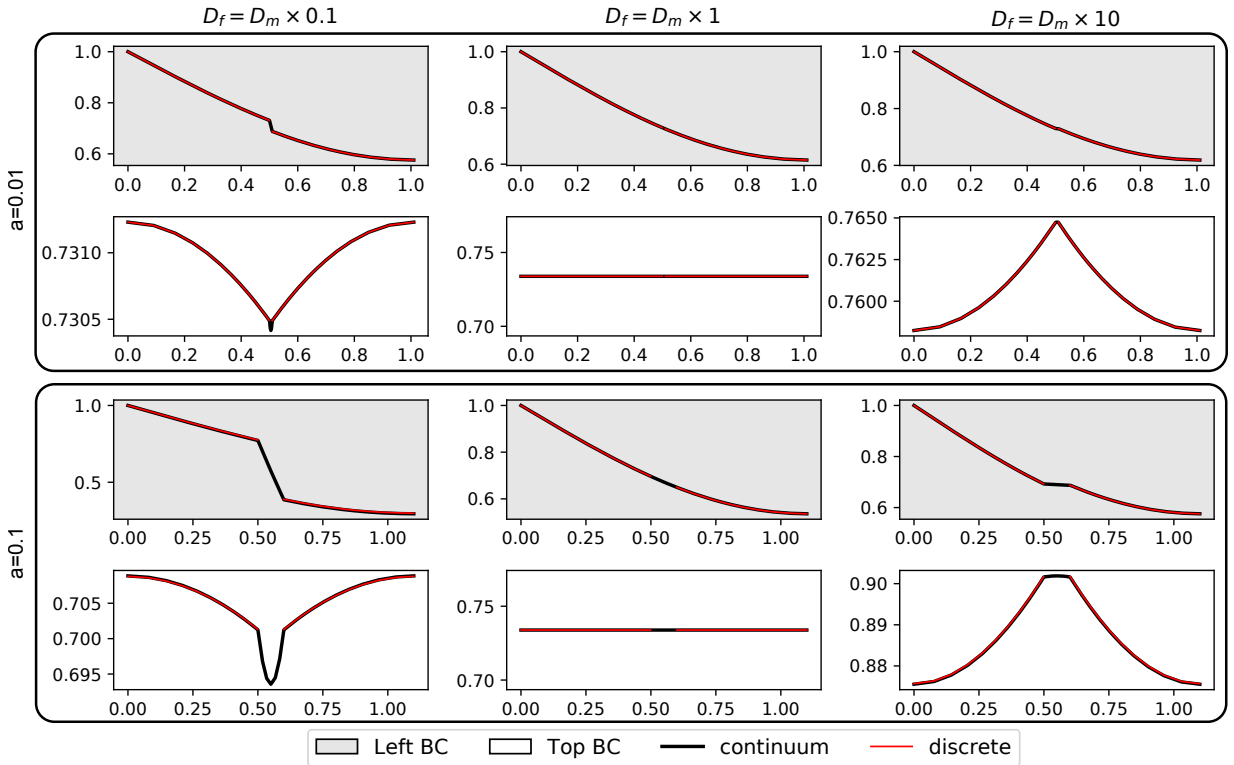


Figure 8: Benchmark profiles for implementation with both interface and lower dimensional blocks. This implementation combines the best of both approaches and matches all cases, even improving on the interface handling for the thicker fault ($a = 0.1$).

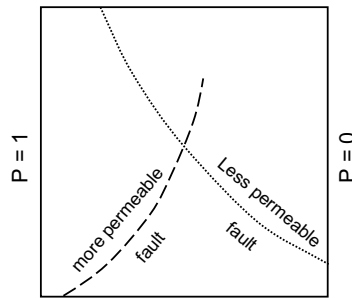


Figure 9: Setup of intersection faults with mixed permeability contrasts, showing the unitary square model, location of the faults and boundary conditions.

311 fault (black curve) is still slowly building up, highlighting the concept that a fault seal is only a relative concept to the
 312 time-scale considered (Wibberley et al., 2008).

313 4. Conclusion

314 In this contribution we presented an accurate method to model impermeable faults bordered by more permeable
 315 damage zones at a larger scale where the overall thickness of those features becomes small enough not to be meshed
 316 as a continuum, hence reducing the computational cost. The method combines the advantages of using lower dimensional
 317 domains, to capture the longitudinal flow in the higher permeability zones, with an interface between duplicated
 318 mesh nodes on the fault to handle the pressure discontinuity. This allows for simultaneously simulating barriers and

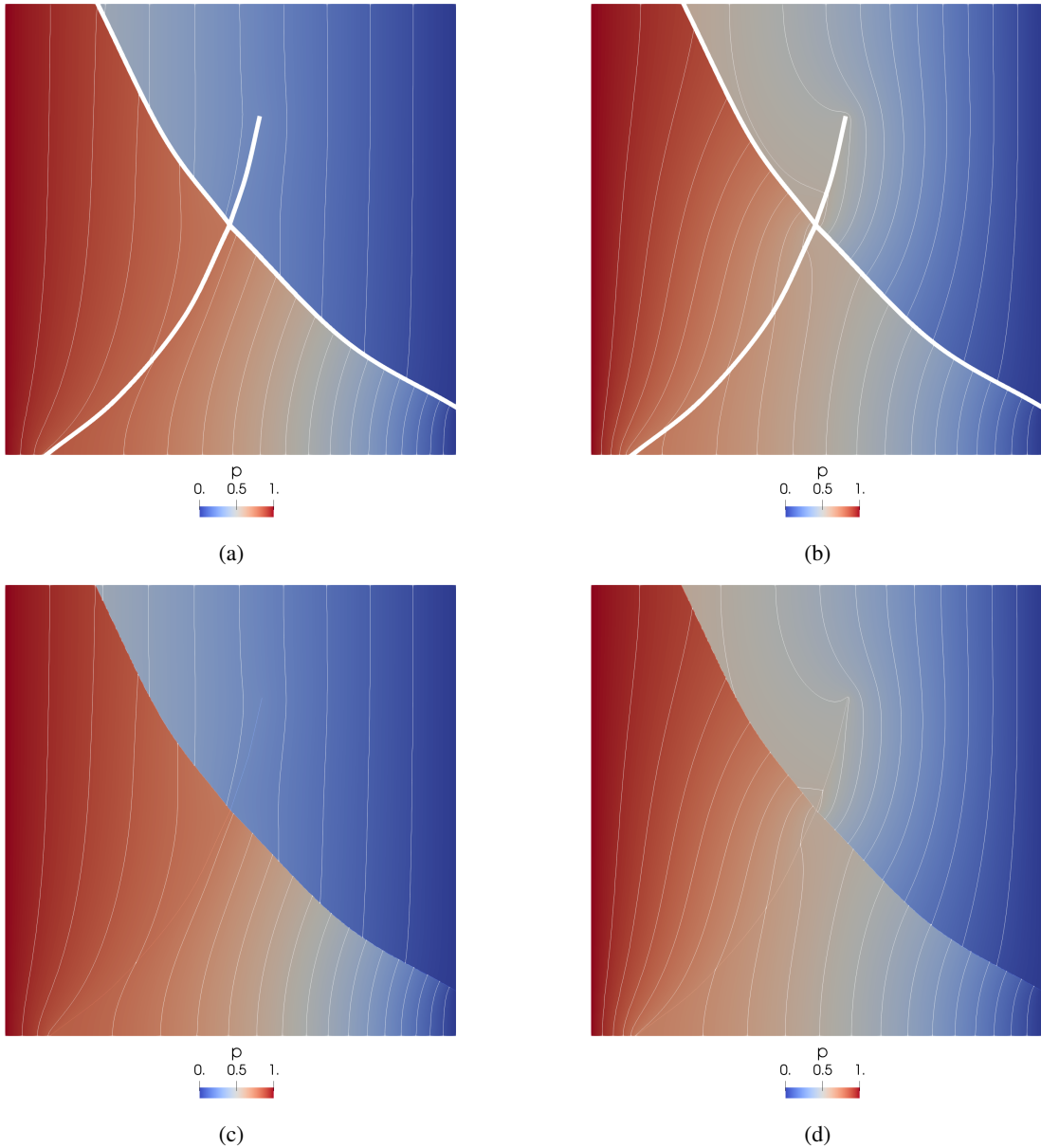


Figure 10: Pressure (p) distributions for two scenarios involving intersecting faults, one with higher and one with lower permeability than the matrix, following Fig. 9, modelled with a continuum (a & b) or discrete (c & d) approach. The first column (a & c) shows the case where the lower permeability fault (downwards from left to right) overprints the higher permeability fault (upwards from left to right). The second column (b & d) shows results for the case where the higher permeability fault overprints the lower permeability one.

319 highly permeable faults, or fractures, and therefore accounting for all structural elements of fault zones. Benchmarks
 320 (Sec. 3.2) showed that our discrete approach provides an accurate representation of the transient (and steady state) hy-
 321 draulic problem on faults of any geometry. Note that the interface method is limited to solving steady-state transversal
 322 flow but in combination with low-dimensional domains allows for solving transient problems as well. Our approach
 323 is also applicable to capturing dynamic permeability evolutions, for instance during fault reactivation (see example
 324 in Sec. 3.4). Finally, we showed how the method can be applied to account for overprinting faults, by treating the
 325 intersections appropriately in the pre-processing step. It is interesting to note that the lower dimensional method is
 326 completely generic as it uses a compelling feature of MOOSE where the system equations is independent of the mesh.

Flow in faulted reservoirs

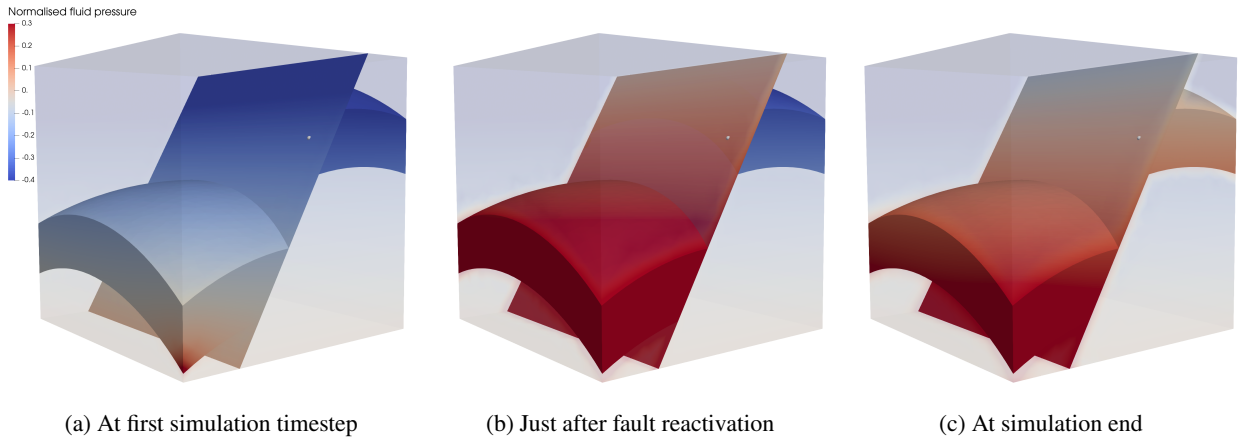


Figure 11: Normalised fluid pressure evolution during reservoir simulation. The pressure builds up first in the lower reservoir, propagates along the fault, and only builds in the upper reservoir after fault reactivation increases the transversal permeability of the fault.

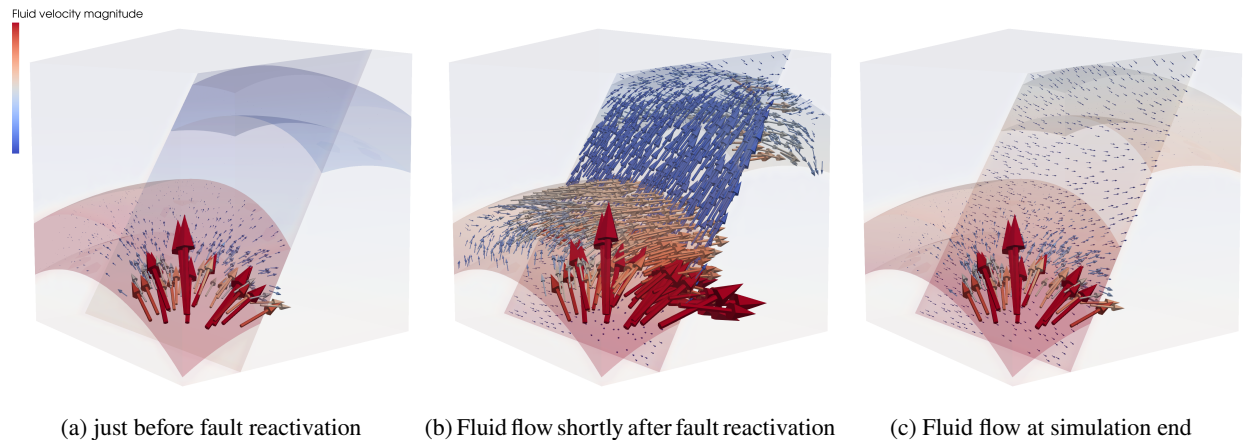


Figure 12: Fluid flow evolution corresponding to scenario shown in Fig. 11. Note that the magnitude of flow arrows is exaggerated ten times in the fault for visualisation purposes (for all three subfigures) and the flow around the source inflow is only shown after a short distance to mask the otherwise overprinting arrows.

327 As such, all existing MOOSE implementations of any physical processes can run natively on lower dimensional do-
328 mains. The interface method, however, requires a specific implementation of the physical processes considered across
329 the discontinuity. We showed here the common case of hydraulic flow with gravity and more physical processes will be
330 added following the same methodology. The simple case of diffusion can already capture scenarios including thermal
331 and hydraulic processes. This paves the way to detailed large scale simulations in various fields including the study
332 of ore deposits, reservoir simulation in faulted environments, fault reactivation, carbon capture and storage, or nuclear
333 waste disposal to name only a few.

334 **Computer code availability**

335 All results presented in this study were obtained with the open-source REDBACK simulator (Poulet et al., 2017)
336 (<http://github.com/pou036/redback>), a MOOSE module (Gaston et al., 2009).

Flow in faulted reservoirs

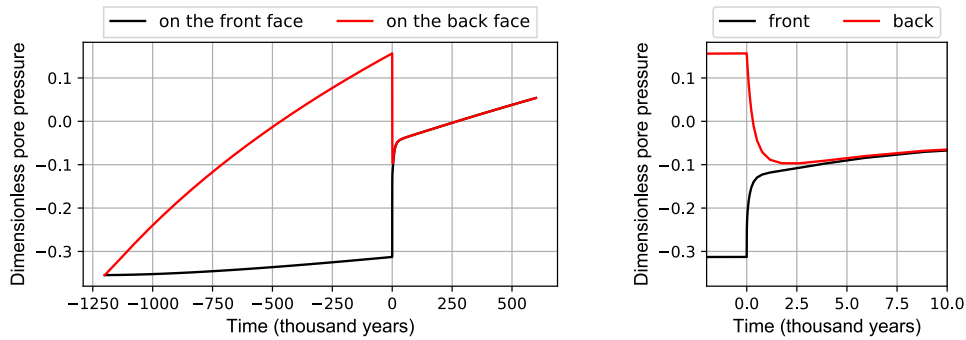


Figure 13: Time evolution of normalised pore pressure at location marked by a grey sphere on Fig. 11, on either sides of the fault, with fault reactivation at $t = 0$; (a) full simulation; (b) zoom on the first 10,000 years after reactivation

References

- 337
- 338 Aben, F.M., Doan, M.L., Gratier, J.P., Renard, F., 2017. Experimental postseismic recovery of fractured rocks assisted by calcite sealing. *Geophysical*
339 *Research Letters* 44, 7228–7238. doi:10.1002/2017GL073965.
- 340 Alboin, C., Jaffré, J., Roberts, J.E., Serres, C., 2002. Modeling fractures as interfaces for flow and transport in porous media, in: Chen, Z., Ewing,
341 R.E. (Eds.), *Fluid Flow and Transport in Porous Media: Mathematical and Numerical Treatment*, American Mathematical Society. pp. 13–24.
342 doi:10.1090/conm/295/04999.
- 343 Alevizos, S., Poulet, T., Veveakis, E., 2014. Thermo-poro-mechanics of chemically active creeping faults. 1: Theory and steady state considerations.
344 *Journal of Geophysical Research: Solid Earth* 119, 4558–4582. doi:10.1002/2013JB010070.
- 345 Angot, P., Boyer, F., Hubert, F., 2009. Asymptotic and numerical modelling of flows in fractured porous media. *ESAIM: Mathematical Modelling*
346 *and Numerical Analysis* 43, 239–275. doi:10.1051/m2an/2008052.
- 347 Barnicoat, A.C., Sheldon, H.A., Ord, A., 2009. Faulting and fluid flow in porous rocks and sediments: implications for mineralisation and other
348 processes. *Mineralium Deposita* 44, 705–718. doi:10.1007/s00126-009-0236-4.
- 349 Bauer, H., Schröckenfuchs, T.C., Decker, K., 2016. Hydrogeological properties of fault zones in a karstified carbonate aquifer (northern calcareous
350 alps, austria). *Hydrogeology Journal* 24, 1147–1170. doi:10.1007/s10040-016-1388-9.
- 351 Bense, V.F., Person, M.A., 2006. Faults as conduit-barrier systems to fluid flow in siliciclastic sedimentary aquifers. *Water Resources Research* 42.
352 doi:10.1029/2005WR004480.
- 353 Berre, I., Doster, F., Keilegavlen, E., 2018. Flow in fractured porous media: A review of conceptual models and discretization approaches. *Transport*
354 *in Porous Media* doi:10.1007/s11242-018-1171-6.
- 355 Cacace, M., Jacquey, A.B., 2017. Flexible parallel implicit modelling of coupled thermal–hydraulic–mechanical processes in fractured rocks. *Solid*
356 *Earth* 8, 921–941. doi:10.5194/se-8-921-2017.
- 357 Caine, J.S., Evans, J.P., Forster, C.B., 1996. Fault zone architecture and permeability structure. *Geology* 24, 1025–1028. doi:10.1130/
358 0091-7613(1996)024<1025:FZAAPS>2.3.CO;2.
- 359 Cappa, F., 2009. Modelling fluid transfer and slip in a fault zone when integrating heterogeneous hydromechanical characteristics in its internal
360 structure. *Geophysical Journal International* 178, 1357–1362. doi:10.1111/j.1365-246X.2009.04291.x.
- 361 Cappa, F., Rutqvist, J., 2011. Modeling of coupled deformation and permeability evolution during fault reactivation induced by deep underground
362 injection of CO₂. *Int. J. Greenhouse Gas Control* 5, 336–346. doi:10.1016/j.ijggc.2010.08.005.
- 363 Cox, S.F., 2016. Injection-driven swarm seismicity and permeability enhancement: Implications for the dynamics of hydrothermal ore systems in
364 high fluid-flux, overpressured faulting regimes - an invited paper. *Economic Geology* 111, 559–587. doi:10.2113/econgeo.111.3.559.
- 365 Faulkner, D., Jackson, C., Lunn, R., Schlische, R., Shipton, Z., Wibberley, C., Withjack, M., 2010. A review of recent developments concerning the
366 structure, mechanics and fluid flow properties of fault zones. *Journal of Structural Geology* 32, 1557–1575. doi:10.1016/j.jsg.2010.06.009.
- 367 Ferronato, M., Gambolati, G., Janna, C., Teatini, P., 2008. Numerical modelling of regional faults in land subsidence prediction above gas/oil
368 reservoirs. *International Journal for Numerical and Analytical Methods in Geomechanics* 32, 633–657. doi:10.1002/nag.640.
- 369 Gasanzade, F., Bauer, S., Pfeiffer, W.T., 2019. Sensitivity analysis of gas leakage through a fault zone during subsurface gas storage in porous
370 formations. *Advances in Geosciences* 49, 155–164. doi:10.5194/adgeo-49-155-2019.
- 371 Gaston, D., Newman, C., Hansen, G., Lebrun-Grandió, D., 2009. Moose: A parallel computational framework for coupled systems of nonlinear
372 equations. *Nuclear Engineering and Design* 239, 1768–1778. doi:10.1016/j.nucengdes.2009.05.021.
- 373 Geuzaine, C., Remacle, J.F., 2009. Gmsh: A 3-d finite element mesh generator with built-in pre- and post-processing facilities. *International Journal*
374 *for Numerical Methods in Engineering* 79, 1309–1331. doi:10.1002/nme.2579.
- 375 Hokr, M., Shao, H., Gardner, W.P., Balvín, A., Kunz, H., Wang, Y., Venci, M., 2016. Real-case benchmark for flow and tracer transport in the
376 fractured rock. *Environmental Earth Sciences* 75. doi:10.1007/s12665-016-6061-z.
- 377 Lesueur, M., 2019. Influence of multiphysics couplings across scales: from digital rock physics to induced fault reactivation. Ph.D. thesis. UNSW
378 Sydney. School of Minerals and Energy Resources Engineering.
- 379 Louis, S., Luijendijk, E., Dunkl, I., Person, M., 2019. Episodic fluid flow in an active fault. *Geology* 47, 938–942. doi:10.1130/G46254.1.
- 380 Martin, V., Jaffré, J., Roberts, J.E., 2005. Modeling fractures and barriers as interfaces for flow in porous media. *SIAM Journal on Scientific*
381 *Computing* 26, 1667–1691. doi:10.1137/S1064827503429363.

- 382 Nguyen, T.S., Guglielmi, Y., Graupner, B., Rutqvist, J., 2019. Mathematical modelling of fault reactivation induced by water injection. *Minerals* 9,
383 282. doi:10.3390/min9050282.
- 384 Poulet, T., Paesold, M., Veveakis, E., 2017. Multi-physics modelling of fault mechanics using redback - a parallel open-source simulator for tightly
385 coupled problems. *Rock Mechanics and Rock Engineering* 50, 733–749. doi:10.1007/s00603-016-0927-y.
- 386 Rawling, G.C., Goodwin, L.B., Wilson, J.L., 2001. Internal architecture, permeability structure, and hydrologic significance of contrasting fault-zone
387 types. *Geology* 29, 43–46. doi:10.1130/0091-7613(2001)029<0043:IAPSAH>2.0.CO;2.
- 388 Schädle, P., Wilkins, A., Ebigbo, A., Saar, M.O., . Flow through an explicitly fractured medium and flow through a fractured network. https://mooseframework.inl.gov/moose/modules/porous_flow/flow_through_fractured_media.html. Accessed: 2019-10-01.
- 389 Schädle, P., Zulian, P., Vogler, D., Bhopalam, S.R., Nestola, M.G., Ebigbo, A., Krause, R., Saar, M.O., 2019. 3d non-conforming mesh model for
390 flow in fractured porous media using lagrange multipliers. *Computers & Geosciences* 132, 42–55. doi:10.1016/j.cageo.2019.06.014.
- 391 Shao, H., He, W., Hokr, M., Gardner, P.W., Kunz, H., Balvin, A., 2016. Flow processes, in: *Thermo-Hydro-Mechanical-Chemical Processes*
392 *in Fractured Porous Media: Modelling and Benchmarking*. Springer International Publishing. *Terrestrial Environmental Sciences*, pp. 33–39.
393 doi:10.1007/978-3-319-29224-3_3.
- 394 Sutherland, R., Toy, V.G., Townend, J., Cox, S.C., Eccles, J.D., Faulkner, D.R., Prior, D.J., Norris, R.J., Mariani, E., Boulton, C., Carpenter, B.M.,
395 Menzies, C.D., Little, T.A., Hasting, M., Pascale, G.P.D., Langridge, R.M., Scott, H.R., Lindroos, Z.R., Fleming, B., Kopf, A.J., 2012. Drilling
396 reveals fluid control on architecture and rupture of the alpine fault, new zealand. *Geology* 40, 1143–1146. doi:10.1130/g33614.1.
- 397 Tillner, E., Langer, M., Kempka, T., Kühn, M., 2016. Fault damage zone volume and initial salinity distribution determine intensity of shallow
398 aquifer salinisation in subsurface storage. *Hydrology and Earth System Sciences* 20, 1049–1067. doi:10.5194/hess-20-1049-2016.
- 399 Tsang, C.F., Neretnieks, I., Tsang, Y., 2015. Hydrologic issues associated with nuclear waste repositories. *Water Resources Research* 51, 6923–6972.
400 doi:10.1002/2015WR017641.
- 401 Veveakis, E., Alevizos, S., Poulet, T., 2017. Episodic tremor and slip (ets) as a chaotic multiphysics spring. *Physics of the Earth and Planetary*
402 *Interiors* 264, 20–34. doi:10.1016/j.pepi.2016.10.002.
- 403 Vrolijk, P.J., Urai, J.L., Kettermann, M., 2016. Clay smear: Review of mechanisms and applications. *Journal of Structural Geology* 86, 95–152.
404 doi:10.1016/j.jsg.2015.09.006.
- 405 Wibberley, C.A.J., Yielding, G., Toro, G.D., 2008. Recent advances in the understanding of fault zone internal structure: a review. *Geological*
406 *Society, London, Special Publications* 299, 5–33. doi:10.1144/sp299.2.
- 407 Yamashita, T., Tsutsumi, A., 2017. Fluid-flow properties of fault zones, in: *Involvement of Fluids in Earthquake Ruptures*. Springer Japan, pp.
408 51–71. doi:10.1007/978-4-431-56562-8_3.
- 409